J. Fluid Mech. (2007), *vol.* 574, *pp.* 85–108. © 2007 Cambridge University Press
doi:10.1017/S0022112006003703 Printed in the United Kingdom

Cooling of a $Pr < 1$ fluid in a rectangular container

WENXIAN LIN[1,3,†], S. W. ARMFIELD[2] AND JOHN C. PATTERSON[1]

[1]School of Engineering, James Cook University, Townsville, QLD 4811, Australia

[2]School of Aerospace, Mechanical and Mechatronic Engineering, The University of Sydney, NSW 2006, Australia

[3]Solar Energy Research Institute, Yunnan Normal University, Kunming 650092, China

(Received 20 January 2006 and in revised form 11 September 2006)

The flow behaviour associated with the cooling of an initially quiescent isothermal Newtonian fluid with Prandtl number Pr less than unity in a rectangular container by unsteady natural convection with an imposed lower temperature on vertical sidewalls is investigated by scaling analysis and direct numerical simulation. The flow is dominated by two distinct stages of development, i.e. the boundary-layer development stage adjacent to the sidewall and the subsequent cooling-down stage. The first stage can be further divided into a start-up stage, transitional stage, and steady-state stage. The parameters characterizing the flow behaviour are the boundary-layer thickness, the maximum vertical velocity within the boundary layer, the time for the boundary layer to reach the steady state, the Nusselt number across the sidewall at the boundary-layer development stage, the time for the fluid in the container to be fully cooled down, and the average fluid temperature over the whole volume of the container.

1. Introduction

The cooling or heating a body of fluid in an enclosure via natural convection with an imposed temperature difference or heat flux on the enclosure boundary is widely encountered in nature and in engineering settings, and the understanding of the transient flow behaviour of such a body of fluid is of fundamental interest and practical importance. In the past decades extensive experimental, numerical, and analytical studies have been conducted on this issue, although mainly on the more specific case of a rectangular cavity with differentially heated sidewalls; see for example the studies reviewed by Catton (1978), Ostrach (1982), Gebhart *et al.* (1988), and Hyun (1994) and those regularly summarized in the annual literature reviews on heat transfer (for example Goldstein *et al.* 2003).

Patterson & Imberger (1980) carried out an investigation of the transient behaviour that occurs when the opposing two vertical sidewalls of a two-dimensional rectangular cavity are impulsively heated and cooled by an equal amount. They devised a classification of the flow development through several transient flow regimes to one of three steady-state types of flow based on the relative values of the Rayleigh number Ra, the Prandtl number Pr, and the aspect ratio A of the cavity. Hyun (1984, 1985) carried out a numerical study which elucidated the flow and temperature structures

† Author to whom correspondence should be addressed: wenxian.lin@jcu.edu.au.

https://doi.org/10.1017/S0022112006003703 Published online by Cambridge University Press

of, and the effect of Pr on, the heat-up process of an initially homogeneous fluid in a cylinder with a linearly heated sidewall using a finite-difference model. Patterson (1984) investigated the transient natural convection in a cavity driven by internal buoyancy sources and sinks distributed linearly in the horizontal and uniformly in the vertical direction using a scaling analysis and found that there are a number of possible transient flow regimes. Nicolette & Yang (1985) made a numerical and experimental investigation into the two-dimensional transient natural convection of single-phase fluids inside a completely filled square enclosure with one vertical wall cooled and the other three walls insulated. Otis & Roessler (1987) conducted an experimental investigation into the development of stratification in a gas in a cylindrical enclosure, provided experimental support for the existence of internal waves, and revealed several time constants that characterize the process. Schladow, Patterson & Street (1989) conducted a series of two- and three-dimensional numerical simulations of transient flow in a side-heated cavity and their simulations generally agree with the results of the scaling arguments of Patterson & Imberger (1980). Patterson & Armfield (1990) conducted detailed experimental and numerical investigations into the presence of travelling-wave instabilities in the vertical-wall boundary layers and horizontal intrusions, revealing the existence of a rapid flow divergence in the region of the outflow of the intrusions and the presence of cavity-scale oscillations caused by the interaction of the intrusion with the opposing vertical boundary layer. Kwak, Kuwahara & Hyun (1998) conducted a numerical study on the transient natural convective cool-down process of a fluid in a cylindrical container, with emphasis on the flow patterns when the maximum-density temperature is reached.

More recently, Lin (2000) and Lin & Armfield (1999, 2001, 2004) investigated the transient processes in the cooling of an initially homogeneous fluid by natural convection in a vertical circular cylinder and in a rectangular container. The results show that vigorous flow activities are concentrated mainly in the vertical thermal boundary layer along the sidewall and in the horizontal region comprising the lower part of the domain where the cold intrusion flow is created. The transient flow patterns at the unsteady and quasi-steady stages were analysed, including the activities of the travelling waves in the vertical thermal boundary layer along the sidewall, the cold intrusion movements in the horizontal region, the stratification of the fluid, and the long-term behaviour beyond full stratification. Various scaling relations characterizing the flow evolution at these distinct development stages were developed by scaling analysis; these were then verified and quantified by extensive direct numerical simulations under different flow situations in terms of Ra, Pr, and A.

The majority of the past studies have focused on fluids with $Pr \geqslant 1$. Studies of natural convection flows with $Pr < 1$ resulting from the heating or cooling of vertical boundaries, especially those in which the long-term behaviour and the effect of Pr variation are examined, have been few. The scarcity of studies on small-Pr fluid flows can be illustrated, as an example, by the seemingly contradictory statements made in the books of Incropera & DeWitt (1996, p. 319), Tritton (1995, p. 170), and Gebhart *et al.* (1988, p. 53). It is stated in the first two books that the viscous boundary layer should be much thinner than the thermal boundary layer when $Pr \ll 1$ whereas in the third book it is argued that both boundary layers should have approximately the same thickness for $Pr < 1$, and even for Pr as small as 0.01. This scarcity, together with the apparently incomplete understanding of $Pr \leqslant 1$ flows, motivates the current study, in which flows with Prandtl numbers in the range $0.01 \leqslant Pr \leqslant 0.5$ are examined. This includes the important cases of gases ($Pr \approx 0.5$) and liquid metals ($Pr \approx 0.01$). In addition to obtaining the behaviour of flows at specific Prandtl numbers, examining

https://doi.org/10.1017/S0022112006003703 Published online by Cambridge University Press

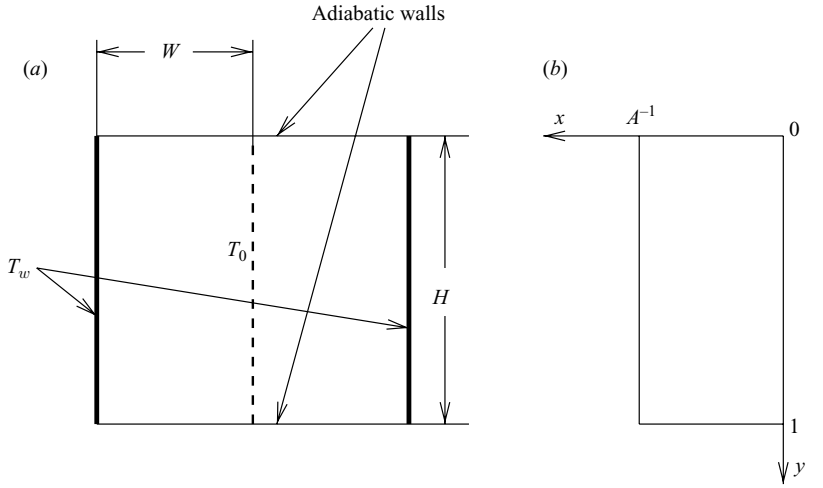


FIGURE 1. (*a*) The physical system considered and (*b*) the appropriate computational domain used for the subsequent numerical simulations. In (*a*), T_0 is the temperature of the fluid at $t = 0$.

and comparing the results for a range of Prandtl numbers will elucidate the governing physics associated with Prandtl-number variation in flows of this type.

In this study, the cooling of an initially quiescent isothermal Newtonian fluid with $Pr < 1$ in a two-dimensional rectangular container by unsteady natural convection with an imposed lower temperature at the vertical sidewalls is investigated by scaling analysis and direct numerical simulation. The scaling analysis is carried out in § 2 in order to develop scaling relations for the parameters characterizing the flow behaviour at different stages of flow development. These scaling relations are then validated and quantified in § 3 by a series of direct numerical simulations with selected values of A, Ra, and Pr in the ranges $1/3 \leqslant A \leqslant 3$, $10^6 \leqslant Ra \leqslant 10^{10}$, and $0.01 \leqslant Pr \leqslant 0.5$. Finally, our conclusions are summarized in § 4.

2. Scaling analysis

Under consideration is the flow behaviour resulting from the cooling of a quiescent isothermal Newtonian fluid with $Pr < 1$ in a two-dimensional rectangular container by unsteady natural convection due to an imposed fixed lower temperature on the vertical sidewalls. The physical system considered in this study and the appropriate computational domain used for the numerical simulations are schematically depicted in figure 1. The container has height H and half-width W. It is assumed that the fluid cools as a result of the imposed fixed temperature T_w on the vertical sidewalls, that all the remaining boundaries are adiabatic, that all boundaries including the sidewalls are non-slip, and that the fluid in the container is initially at rest and at a uniform temperature T_0 ($T_0 > T_w$). It is also assumed that the flows are laminar and that symmetry allows one-half of the physical domain to be chosen as the computational domain, as shown in figure 1(*b*).

The governing equations of motion are the Navier–Stokes equations with the Boussinesq approximation for buoyancy, which together with the temperature

https://doi.org/10.1017/S0022112006003703 Published online by Cambridge University Press

transport equation can be written in the following two-dimensional form:

$$\frac{\partial U}{\partial X}+\frac{\partial V}{\partial Y}=0, \tag{2.1}$$

$$\frac{\partial U}{\partial t}+\frac{\partial (UU)}{\partial X}+\frac{\partial (VU)}{\partial Y}=-\frac{1}{\rho}\frac{\partial P}{\partial X}+\nu\left(\frac{\partial^2 U}{\partial X^2}+\frac{\partial^2 U}{\partial Y^2}\right), \tag{2.2}$$

$$\frac{\partial V}{\partial t}+\frac{\partial (UV)}{\partial X}+\frac{\partial (VV)}{\partial Y}=-\frac{1}{\rho}\frac{\partial P}{\partial Y}+\nu\left(\frac{\partial^2 V}{\partial X^2}+\frac{\partial^2 V}{\partial Y^2}\right)-g\beta(T-T_0), \tag{2.3}$$

$$\frac{\partial T}{\partial t}+\frac{\partial (UT)}{\partial X}+\frac{\partial (VT)}{\partial Y}=\kappa\left(\frac{\partial^2 T}{\partial X^2}+\frac{\partial^2 T}{\partial Y^2}\right). \tag{2.4}$$

Here U and V are the horizontal (X-direction) and vertical (Y-direction) velocity components, t is the time, P is the pressure, T is the temperature, g is the acceleration due to gravity, and β, ν, and κ are the thermal expansion coefficient, kinematic viscosity, and thermal diffusivity of the fluid, respectively. Gravity acts in the Y-direction.

It is found from the numerical simulations that the flow considered here is dominated by two distinct stages of development, i.e. a boundary-layer development stage and a cooling-down stage. The typical flow development is illustrated in figure 2, where numerically simulated temperature contours in half the container are shown for the two stages for the specific case of $Ra=10^8$, $A=1$ and $Pr=0.1$, where Ra, Pr, and A are defined as follows:

$$Ra=\frac{g\beta(T_0-T_w)H^3}{\nu\kappa}, \qquad Pr=\frac{\nu}{\kappa}, \qquad A=\frac{H}{W}.$$

In this case the boundary-layer development is seen in the temperature contours adjacent to the right-hand cooled wall; the boundary-layer development is complete by around $\tau=10$, where τ is the time made dimensionless by H/V_0. Here V_0 is the characteristic velocity, which will be defined in (3.5) below. The cooled fluid ejected by the boundary layer acts to fill and stratify the domain from $\tau=35$ to 125, the average temperature gradually reducing in the subsequent cooling-down stage of the flow, at $\tau>225$. In this section, scaling relations will be developed for the relevant parameters characterizing the flow behaviour at these respective stages of flow development.

2.1. *Boundary-layer development stage*

With the initiation of the flow, a vertical boundary layer is developed adjacent to the cooled sidewall. It will experience a start-up stage dominated by one-dimensional conduction, followed by a short transitional stage at which the one-dimensional conduction transits to a two-dimensional convection, and finally a steady-state stage. The parameters characterizing the flow behaviour at the boundary layer's development stage are predominantly the thermal boundary-layer thickness Δ_T, the maximum vertical velocity V_m within the boundary layer, the time $t_{s,Y}$ for the boundary layer at location Y to reach the steady state, the local Nusselt number Nu_Y, and the global Nusselt number Nu along the whole sidewall, as illustrated in figure 3, where typical numerically simulated time series for $\delta_T=\Delta_T/H$, $v_m=V_m/V_0$, the local Nusselt number Nu_y at height $y=0.5$, and the global Nusselt number Nu along the whole sidewall are presented. The thermal boundary-layer thickness Δ_T is defined as the horizontal distance between the sidewall and the location where the fluid temperature reaches $0.01(T_w-T_0)$. The time $\tau_{s,y}$ for the boundary-layer development to reach the steady state, which is made dimensionless by H/V_0, is determined by the moment when Δ_T ceases to change with time: the criterion for the determination of

https://doi.org/10.1017/S0022112006003703 Published online by Cambridge University Press

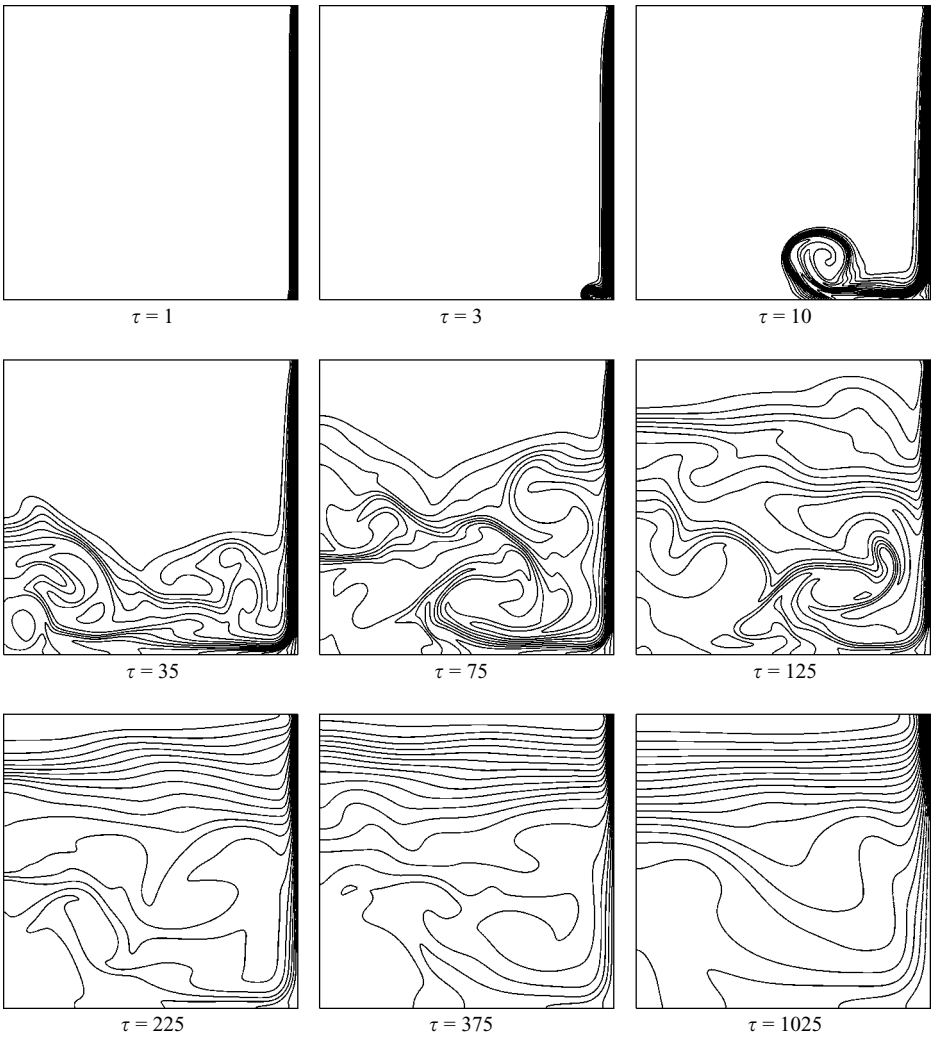


FIGURE 2. Numerically simulated temperature contours at the boundary-layer development stage (top row) and at the cooling-down stage (middle and bottom rows), for $Ra = 10^8$, $A = 1$, and $Pr = 0.1$; τ is made dimensionless by H/V_0.

$\tau_{s,y}$ used in the numerical simulations was that the difference between $\Delta_T(\tau_{s,y})$ and its value at the previous time step had dropped to 0.01 %.

Scalings for these quantities may be developed as follows. Heat is initially transferred out through the vertical wall from the fluid by pure conduction immediately after the initiation of the flow, resulting in a one-dimensional vertical thermal boundary layer adjacent to the wall. Consider first the temperature equation (2.4). The unsteady term is $O(\Delta T/t)$, where t is the time scale and $\Delta T = T_w - T_0$. The convective terms are $O(V\Delta T/H)$ and the conduction terms are $O(\Delta T/\Delta_T^2)$, where Δ_T is the horizontal length scale for the thermal boundary layer.

Compare the magnitudes of the first and third terms on the left-hand side of (2.4):

$$\frac{\text{unsteady term}}{\text{convection term}} \sim \frac{\Delta T/t}{V\Delta T/H} \sim \frac{H}{Vt}. \tag{2.5}$$

https://doi.org/10.1017/S0022112006003703 Published online by Cambridge University Press

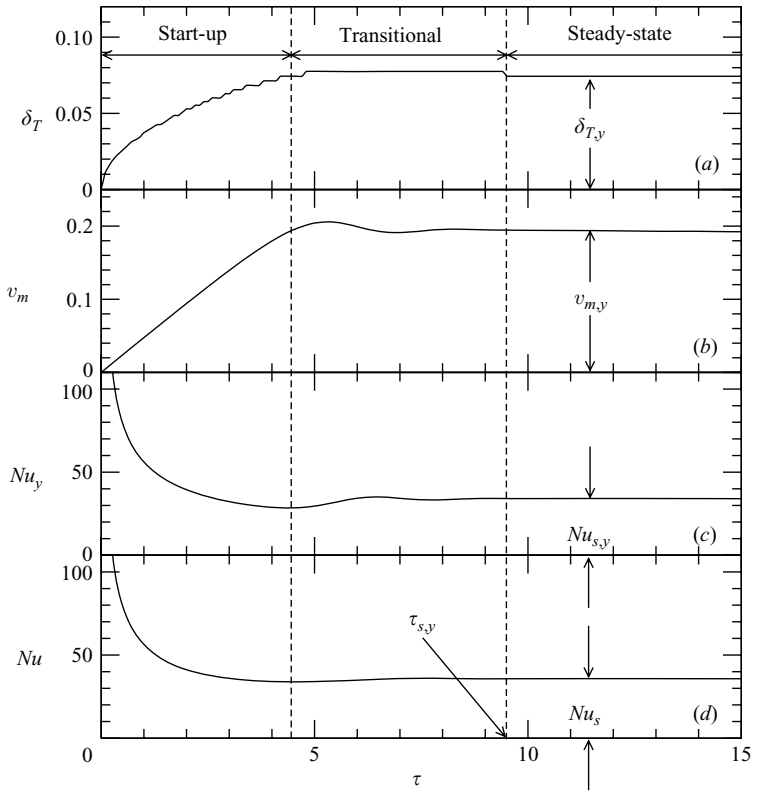


FIGURE 3. The three distinct substages in the boundary-layer development stage, seen in the numerically simulated typical time series of (*a*) the local thermal boundary-layer thickness $\delta_T = \Delta_T/H$ at height $Y = 0.5H$; (*b*) the local maximum vertical velocity $v_m = V_m/V_0$ at $Y = 0.5H$; (*c*) the local Nusselt number Nu_y at $Y = 0.5H$; and (*d*) the global Nusselt number Nu along the vertical sidewall, for the specific case $Ra = 10^8$, $Pr = 0.1$, and $A = 1$; τ is made dimensionless by H/V_0.

We can always find a time t small enough that $H/(Vt) \gg 1$, so that the appropriate balance becomes

$$\frac{\partial T}{\partial t} \sim \kappa \frac{\partial^2 T}{\partial X^2}, \tag{2.6}$$

giving

$$\frac{\Delta T}{t} \sim \kappa \frac{\Delta T}{\Delta_T^2} \tag{2.7}$$

or

$$\Delta_T \sim \kappa^{1/2} t^{1/2}. \tag{2.8}$$

This is valid until the convective term becomes important or the steady state is reached.

Now consider the vertical momentum equation (2.3). The unsteady term is $O(V/t)$, the advection terms are $O(V^2/H)$, the viscous terms are $O(\nu V/\Delta_T^2)$, and the forcing term is $O(g\beta\Delta T)$. The ratio of the unsteady and advection terms is $(V/t)/(V^2/H) \sim H/(Vt)$ and the ratio of the unsteady and viscous terms is $(V/t)/(\nu V/\Delta_T^2) \sim \Delta_T^2/(\nu t) \sim 1/Pr$. We can always find a t small enough that the unsteady term is larger than the advection term, and the other ratio depends on the

https://doi.org/10.1017/S0022112006003703 Published online by Cambridge University Press

value of Pr. For $Pr \gg 1$ the viscous term is much larger than the unsteady term, and the correct balance is between the viscous term and the buoyancy term $g\beta\Delta T$ (Patterson & Imberger 1980). For $Pr \ll 1$ the unsteady term is much larger than the viscous term, and the correct balance is between the unsteady and buoyancy terms. If $Pr \sim O(1)$ then the unsteady and viscous terms are of the same order and both need to be included in a balance with the buoyancy term.

The unsteady term is $O(V/t)$ and the viscous term is $O(PrV/t)$, so these two terms together are $O((1+Pr)V/t)$ and now the balance in the vertical momentum equation is

$$(1 + Pr)\frac{V}{t} \sim g\beta\Delta T, \tag{2.9}$$

giving

$$V_m \sim \frac{g\beta\Delta T t}{1 + Pr}. \tag{2.10}$$

Now consider the time taken to get to the steady state. The approach is to find the time when convection is important, i.e. when

$$V_m \frac{\partial T}{\partial y} \sim \frac{\partial T}{\partial t}, \tag{2.11}$$

so that at location Y we have

$$V_m \frac{\Delta T}{Y} \sim \frac{\Delta T}{t_{s,Y}}, \tag{2.12}$$

or

$$V_m t_{s,Y} \sim Y. \tag{2.13}$$

From (2.10), this gives

$$\frac{g\beta\Delta T t_{s,Y}}{1 + Pr} t_{s,Y} \sim Y, \tag{2.14}$$

so that

$$t_{s,Y} \sim \frac{Y^{1/2}(1 + Pr)^{1/2}}{(g\beta\Delta T)^{1/2}}, \tag{2.15}$$

i.e.

$$t_{s,Y} \sim \frac{Y^{1/2}H^{3/2}(1 + Pr)^{1/2}}{Ra^{1/2}Pr^{1/2}\kappa}. \tag{2.16}$$

The result for $Y \sim H$, i.e. the final steady state for the boundary layer, is obtained by putting $Y \sim H$ in (2.16), to get

$$t_{s,H} \sim \frac{H^2(1 + Pr)^{1/2}}{Ra^{1/2}Pr^{1/2}\kappa}. \tag{2.17}$$

So, the steady state in the boundary layer occurs at $t_{s,H}$. At that time the thermal boundary layer at height Y is, from (2.8), given by

$$\Delta_{T,Y} \sim \kappa^{1/2} t_{s,Y}^{1/2} \sim \frac{H^{3/4}Y^{1/4}(1 + Pr)^{1/4}}{Ra^{1/4}Pr^{1/4}}, \tag{2.18}$$

and at the steady state for the whole boundary layer, i.e. when $Y \sim H$, we have

$$\Delta_{T,H} \sim \frac{H}{Ra^{1/4}}\left(\frac{1 + Pr}{Pr}\right)^{1/4}. \tag{2.19}$$

https://doi.org/10.1017/S0022112006003703 Published online by Cambridge University Press

As the upper limit of $\Delta_{T,H}$ is W, this requires

$$\frac{H}{Ra^{1/4}}\left(1+\frac{1}{Pr}\right)^{1/4} < W, \tag{2.20}$$

which in turn requires

$$Pr > \left(\frac{Ra}{A^4}-1\right)^{-1}. \tag{2.21}$$

This is the lower limit of Pr that will guarantee the validity of the scaling relations obtained in this scaling analysis. As all these scaling relations are obtained under the assumption $Pr < O(1)$, the upper limit of Pr is then $O(1)$, leading to the requirement that $Ra > A^4$.

The steady vertical velocity at distance Y is, using $t_{s,Y}$ from (2.13),

$$V_{m,Y} \sim \frac{Y}{t_{s,Y}} \sim \frac{Y^{1/2}Ra^{1/2}\kappa}{H^{3/2}}\left(\frac{Pr}{1+Pr}\right)^{1/2}. \tag{2.22}$$

Again the whole boundary layer is steady when $Y \sim H$ and

$$V_{m,H} \sim \frac{\kappa Ra^{1/2}}{H}\left(\frac{Pr}{1+Pr}\right)^{1/2}. \tag{2.23}$$

A scaling for the viscous boundary-layer thickness may be developed in a manner analogous to that of $\Delta_{T,Y}$. From (2.3), $\Delta_v \sim (\nu t)^{1/2}$ and from (2.8) it is found that

$$\Delta_{vi,Y} = Pr^{1/2}\Delta_{T,Y}, \tag{2.24}$$

indicating that for $Pr < 1$ the region over which there is a balance between the vertical acceleration and viscous diffusion of momentum, i.e. the near-wall region, is smaller than the corresponding thermal-conduction region; the subscript i denotes this inner region. The vertical velocity boundary layer therefore comprises two regions, a near-wall region governed by the wall conditions (2.24) and an outer region in which the flow is governed by a balance between vertical acceleration and buoyancy determined by the extent of the thermal boundary layer, i.e.

$$\Delta_{vo,Y} \approx \Delta_{T,Y}. \tag{2.25}$$

The inner boundary-layer width Δ_{vi} is the region selected by Incropera & DeWitt (1996, p. 319) and Tritton (1995, p. 170) to represent the velocity boundary-layer width, while the outer boundary-layer width Δ_{vo} is the region selected by Gebhart *et al.* (1988, p. 53) to represent the velocity boundary-layer width.

The instantaneous local Nusselt number at distance Y on the wall during the boundary-layer development stage is

$$Nu_Y \sim \frac{(\partial T/\partial X)_{X=0}}{\Delta T/W} \sim \frac{W}{\Delta T}\frac{\Delta T}{\Delta_T} \sim \frac{W}{\kappa^{1/2}t^{1/2}}. \tag{2.26}$$

At steady state, from (2.16) the local Nusselt number becomes

$$Nu_{s,Y} \sim \frac{WRa^{1/4}}{H^{3/4}Y^{1/4}}\frac{Pr^{1/4}}{(1+Pr)^{1/4}}. \tag{2.27}$$

The average steady-state Nu for the whole boundary layer is given by

$$Nu_s \sim \frac{1}{H}\int_0^H Nu_{s,Y}\,\mathrm{d}Y \sim \frac{W}{H}Ra^{1/4}\left(\frac{Pr}{1+Pr}\right)^{1/4}. \tag{2.28}$$

https://doi.org/10.1017/S0022112006003703 Published online by Cambridge University Press

2.2. *Cooling-down stage*

Once the boundary layer is fully developed, the fluid in the container is gradually stratified by the cooled fluid ejected from the boundary layer, starting from the bottom of the container, and this cooling-down stage continues until the whole body of fluid has the same temperature as that imposed on the sidewalls. The appropriate parameters to characterize this cooling-down stage are the time t_f for the fluid to be fully cooled down, the average fluid temperature $T_a(t)$ over the whole volume of the container per unit length at time t, and the average Nusselt number at the cooling wall.

Let us consider any specific moment t during the cooling-down stage. At that moment, the fluid inside the container can be assumed to consist of two layers with the location $Y = Y_i$ as the interface. The top layer has the original temperature, T_0, whereas the bottom layer has the wall temperature T_w. Mass conservation then requires

$$W\frac{\mathrm{d}(H - Y_i)}{\mathrm{d}t} \sim V_{m,Y_i}\Delta_{T,Y_i}, \tag{2.29}$$

which, with (2.18) and (2.22), gives

$$\frac{\mathrm{d}Y_i}{Y_i^{3/4}} \sim -\frac{\kappa Ra^{1/4}}{WH^{3/4}}\left(\frac{Pr}{1+Pr}\right)^{1/4}\mathrm{d}t. \tag{2.30}$$

Using the facts that $Y_i = H$ when $t = 0$ and $Y_i = 0$ when $t = t_f$, the solution to the above equation is

$$Y_i \sim \frac{\kappa^4 Ra}{W^4H^3}\left(\frac{Pr}{1+Pr}\right)(t_f - t)^4, \tag{2.31}$$

which gives

$$t_f \sim \frac{HW}{\kappa Ra^{1/4}}\left(\frac{1+Pr}{Pr}\right)^{1/4}. \tag{2.32}$$

The average fluid temperature $T_a(t)$ is given by

$$\begin{aligned} T_a(t) &= \frac{(H - Y_i)T_w + Y_iT_0}{H} = T_w + (T_0 - T_w)\frac{Y_i}{H} \\ &= T_w + (T_0 - T_w)C_f\frac{\kappa^4 Ra}{W^4H^3}\left(\frac{Pr}{1+Pr}\right)(t_f - t)^4, \end{aligned} \tag{2.33}$$

where C_f is a constant of proportionality which will be determined below from the numerical results.

It is apparent from (2.28) that the instantaneous global Nusselt number Nu at the cooling-down stage is

$$Nu \sim \left(\frac{Y_i}{H}\right)Nu_{s,Y_i}, \tag{2.34}$$

which, from (2.27) and (2.31), gives

$$Nu \sim \frac{\kappa^3 Ra}{AW^3H^3}\left(\frac{Pr}{1+Pr}\right)(t_f - t)^3. \tag{2.35}$$

3. Numerical results

In this section, the scaling relations obtained above will be validated and quantified by a series of direct numerical simulations with selected values of A, Ra, and Pr in

https://doi.org/10.1017/S0022112006003703 Published online by Cambridge University Press

Run no.	A	Ra	Pr
1	1	10^6	0.1
2	1	10^7	0.1
3	1	10^8	0.1
4	1	10^9	0.1
5	1	10^{10}	0.1
6	1	10^8	0.01
7	1	10^8	0.05
8	1	10^8	0.5
9	1/3	10^8	0.1
10	1/2	10^8	0.1
11	2	10^8	0.1
12	3	10^8	0.1

TABLE 1. Values of A, Ra, and Pr for the 12 DNS runs.

the ranges $1/3 \leqslant A \leqslant 3$, $10^6 \leqslant Ra \leqslant 10^{10}$, and $0.01 \leqslant Pr \leqslant 0.5$. A total of 12 DNS runs were carried out for this purpose, as shown in table 1. Specifically, runs 1–5 with $Ra = 10^6$, 10^7, 10^8, 10^9, and 10^{10}, keeping $A = 1$ and $Pr = 0.1$, were carried out to show the dependence of the scaling relations on Ra; runs 6, 7, 3, and 8 with, respectively, $Pr = 0.01$, 0.05, 0.1, and 0.5, keeping $Ra = 10^8$ and $A = 1$, were carried out to show the dependence on Pr; and runs 9, 10, 3, 11 and 12 with, respectively, $A = 1/3$, $1/2$, 1, 2, and 3, keeping $Ra = 10^8$ and $Pr = 0.1$, were carried out to show the dependence on A.

3.1. *Governing equations, initial and boundary conditions, and scaling relations in dimensionless form*

The governing equations (2.2)–(2.4) can be expressed in the following dimensionless forms:

$$\frac{\partial u}{\partial x} + \frac{\partial v}{\partial y} = 0, \tag{3.1}$$

$$\frac{\partial u}{\partial \tau} + \frac{\partial (uu)}{\partial x} + \frac{\partial (vu)}{\partial y} = -\frac{\partial p}{\partial x} + \frac{Pr}{Ra^{1/2}} \left(\frac{\partial^2 u}{\partial x^2} + \frac{\partial^2 u}{\partial y^2} \right), \tag{3.2}$$

$$\frac{\partial v}{\partial \tau} + \frac{\partial (uv)}{\partial x} + \frac{\partial (vv)}{\partial y} = -\frac{\partial p}{\partial y} + \frac{Pr}{Ra^{1/2}} \left(\frac{\partial^2 v}{\partial x^2} + \frac{\partial^2 v}{\partial y^2} \right) - Pr\theta, \tag{3.3}$$

$$\frac{\partial \theta}{\partial \tau} + \frac{\partial (u\theta)}{\partial x} + \frac{\partial (v\theta)}{\partial y} = \frac{1}{Ra^{1/2}} \left(\frac{\partial^2 \theta}{\partial x^2} + \frac{\partial^2 \theta}{\partial y^2} \right), \tag{3.4}$$

Here x, y, u, v, τ, p, and θ are respectively the dimensionless forms of X, Y, U, V, t, P, and T:

$$x = \frac{X}{H}, \quad y = \frac{Y}{H}, \quad u = \frac{U}{V_0}, \quad v = \frac{V}{V_0}, \quad \tau = \frac{t}{(H/V_0)}, \quad p = \frac{P}{\rho V_0^2}, \quad \theta = \frac{T - T_0}{T_0 - T_w}$$

with V_0, H, H/V_0, ρV_0^2 respectively the characteristic velocity, length, time, and pressure scales. From (2.23), it is natural to choose

$$V_0 = \kappa Ra^{1/2}/H \tag{3.5}$$

as the appropriate characteristic velocity scale.

https://doi.org/10.1017/S0022112006003703 Published online by Cambridge University Press

The appropriate initial and boundary conditions are

$$u = v = 0,\ \theta = 0 \text{ at all } x,\ y \text{ for } \tau < 0;$$
$$u = 0,\ \frac{\partial v}{\partial x} = 0,\ \frac{\partial \theta}{\partial x} = 0 \text{ at } x = 0,\ 0 \leqslant y \leqslant 1;$$
$$u = v = 0,\ \theta = -1 \text{ at } x = A^{-1},\ 0 \leqslant y \leqslant 1;$$
$$u = v = 0,\ \frac{\partial \theta}{\partial y} = 0 \text{ at } 0 \leqslant x \leqslant A^{-1},\ y = 0;$$
$$u = v = 0,\ \frac{\partial \theta}{\partial y} = 0 \text{ at } 0 \leqslant x \leqslant A^{-1},\ y = 1, \text{ for } \tau \geqslant 0.$$

The scaling relations given in § 2 can be made dimensionless using H and V_0. During the start-up stage of boundary-layer development the scaling relations (2.8), (2.10), and (2.26) can be written in dimensionless form as

$$\delta_T = \frac{\Delta_T}{H} \sim \frac{\tau^{1/2}}{Ra^{1/4}}, \tag{3.6}$$

$$v_m = \frac{V_m}{V_0} \sim \left(\frac{Pr}{1+Pr}\right)\tau, \tag{3.7}$$

$$Nu_y \sim \frac{W}{(\kappa t)^{1/2}} \sim \frac{W}{H\delta_T} \sim \frac{Ra^{1/4}}{A\tau^{1/2}}, \tag{3.8}$$

and at the steady-state stage of boundary-layer development the scaling relations (2.16)–(2.18), (2.22), (2.24), (2.25), (2.27), and (2.28) can be written in dimensionless forms as

$$\tau_{s,y} = \frac{t_{s,Y}}{H/V_0} \sim \left(\frac{1+Pr}{Pr}\right)^{1/2} y^{1/2}, \tag{3.9}$$

$$\tau_{s,1} = \frac{t_{s,H}}{H/V_0} \sim \left(\frac{1+Pr}{Pr}\right)^{1/2}, \tag{3.10}$$

$$\delta_{T,y} = \frac{\Delta_{T,Y}}{H} \sim \left(\frac{1+Pr}{Pr}\right)^{1/4} \frac{y^{1/4}}{Ra^{1/4}}, \tag{3.11}$$

$$v_{m,y} = \frac{V_{m,Y}}{V_0} \sim \left(\frac{Pr}{1+Pr}\right)^{1/2} y^{1/2}, \tag{3.12}$$

$$\delta_{vi,y} = \frac{\Delta_{vi,Y}}{H} \sim Pr^{1/2}\delta_{T,y} \sim Pr^{1/4}(1+Pr)^{1/4}\frac{y^{1/4}}{Ra^{1/4}}, \tag{3.13}$$

$$\delta_{vo,y} = \frac{\Delta_{vo,Y}}{H} \approx \delta_{T,y} \sim \left(\frac{1+Pr}{Pr}\right)^{1/4} \frac{y^{1/4}}{Ra^{1/4}}, \tag{3.14}$$

$$Nu_{s,y} \sim \frac{Ra^{1/4}}{Ay^{1/4}} \left(\frac{Pr}{1+Pr}\right)^{1/4}, \tag{3.15}$$

$$Nu_s \sim \frac{Ra^{1/4}}{A} \left(\frac{Pr}{1+Pr}\right)^{1/4}. \tag{3.16}$$

Equations (3.6)–(3.8) clearly show that during the start-up stage the boundary-layer development on the vertical sidewalls is one-dimensional and independent of y, owing

https://doi.org/10.1017/S0022112006003703 Published online by Cambridge University Press

to the dominance of pure conduction. However, at the steady-state stage, as shown by (3.11), (3.12), and (3.15), the boundary-layer development and the heat transfer across the vertical sidewall become two-dimensional and y-dependent as the flow is now dominated by convection.

The scaling relation (2.32) for the cooling-down time t_f can be written in dimensionless form as

$$\tau_f = \frac{t_f}{H/V_0} \sim \left(\frac{1+Pr}{Pr}\right)^{1/4} \frac{Ra^{1/4}}{A}, \tag{3.17}$$

and the decay of the average dimensionless fluid temperature $\theta_a(\tau)$, becomes from (2.33)

$$\theta_a(\tau) = C_f \frac{A^4}{Ra}\left(\frac{Pr}{1+Pr}\right)(\tau_f - \tau)^4 - 1. \tag{3.18}$$

From (2.35), it is found that the instantaneous global Nusselt number Nu at the cooling-down stage is

$$Nu \sim \frac{Ra^{1/4}}{A}\left(\frac{Pr}{1+Pr}\right)^{1/4}\left(1 - \frac{\tau}{\tau_f}\right)^3. \tag{3.19}$$

3.2. *Numerical method*

Detailed information about the numerical algorithm and numerical accuracy tests can be found in Lin & Armfield (1999) and Lin (2000). Only a brief description is given here.

The governing equations are discretized on a non-staggered mesh using finite volumes, standard second-order central-difference schemes being used for the viscous, pressure-gradient, and divergence terms. The QUICK third-order upwind scheme was used for the advective terms (Leonard 1979). The second-order Adams–Bashforth scheme and the Crank–Nicolson scheme were used for the time integration of the advective terms and the diffusive terms, respectively. To enforce the continuity, the pressure-correction method was used to construct a Poisson equation, which was solved using the preconditioned GMRES method. Detailed descriptions of these schemes are given in Armfield (1991) and Armfield & Street (1999), and the code has been widely used for the simulation of a range of buoyancy-dominated flows (see e.g. Patterson & Armfield 1990; Armfield & Debler 1993; Javam, Imberger & Armfield 1999; Lin & Armfield 2000, 2001, 2002, 2003, 2004).

Owing to the large variation in length scales it is necessary to use a computational mesh that concentrates points in the boundary layer and is relatively coarse in the interior. In this study, the meshes used for all runs were constructed using a stretched grid, with nodes distributed symmetrically with respect to the half-width and half-height of the computational domain represented by figure 1(*b*). The basic mesh used for runs 1–8 had 299×299 grid points and the nearest grid point was located 0.0001 from the domain boundaries. Subsequently, the mesh was allowed to expand at a fixed rate of 4.01 % up to $x = y = 0.1$ in both x- and y-directions. After that, the mesh-size expansion rate decreased at a rate of 10 % until it reached zero, resulting in a constant coarser mesh in the interior of the domain. The meshes for runs 9–12 were constructed in a similar fashion but with different mesh-size expansion rates in the y-direction, i.e. 6.05 %, 6.1 %, 4.01 %, and 4.1 %, resulting in 399×299, 297×299, 249×299, and 219×299 grid points, respectively.

https://doi.org/10.1017/S0022112006003703 Published online by Cambridge University Press

To determine whether any three-dimensional or asymmetric effects were present, three-dimensional solutions were also obtained on the full domain with $0 \leqslant x \leqslant 2$, $0 \leqslant y \leqslant 1$, and $0 \leqslant z \leqslant 1$, where z is the spanwise direction. The three-dimensional solutions were obtained with a non-uniform grid of 228×194 nodes in the x- and y-directions. Both the periodic and wall-boundary conditions (zero velocity and zero normal temperature gradient) were applied to the spanwise boundaries $z = 0$, 1. The smallest grid sizes in the x- and y-directions were $\Delta x = \Delta y = 5 \times 10^{-4}$ with a mesh-size expansion rate of 4 %. For the periodic boundary conditions, 50 uniformly spaced nodes were used in the z-direction; for the wall boundaries a non-uniform grid was used with minimum grid spacing 5×10^{-4} at the walls and a mesh-size expansion rate of 4 %, giving 194 nodes in the z-direction. The time-step size was $\Delta\tau = 2 \times 10^{-4}$. The use of a coarser grid and a larger time step for the three-dimensional simulations, as compared with the two-dimensional simulations, was necessary, owing to computational limitations, to enable results to be obtained in a reasonable time. The specific case $Ra = 10^{10}$, $A = 1$, and $Pr = 0.1$ was chosen, as in this extreme case the asymmetrical and/or three-dimensional effects, if they exist, will most likely occur. The solution with periodic boundary conditions was found to have no spanwise, z, variation and to be symmetric about the plane $x = 1$. The solution with wall-boundary conditions on the spanwise boundaries is three-dimensional as a result of the boundary layers generated on the spanwise walls. These boundary layers have a negligible effect on the natural-convection boundary layers that form on the cooled walls, and lead to the generation of some three-dimensional structures in the filling flow in the interior of the container. Although this affects the detailed structure of the filling flow, the scaled quantities examined here, such as the natural-convection boundary-layer start-up time, the boundary-layer thickness, and the total filling time, are not affected. Similar results were obtained when an initial random perturbation was included in the solution. The use of two-dimensional and symmetric simulations to validate the scaling relations and provide scaling constants is therefore appropriate. The code was further validated against the one-dimensional transient natural-convection boundary-layer solution of Goldstein & Briggs (1964) and against the two-dimensional steady-state similarity solution of Ostrach (1952), for small Prandtl number; it was shown to accurately predict these flows.

3.3. *Numerical validation and quantification of the scaling relations*

3.3.1. *Boundary-layer development stage*

Numerical results showing the scaling relations at the steady-state stage of the boundary-layer development, i.e. (3.9), (3.11), (3.12), (3.15), and (3.16), are presented in figures 4 and 5, where it is seen that these direct numerical simulation results agree very well with the scaling relations for A, Ra, and Pr in the ranges $1/3 \leqslant A \leqslant 3$, $10^6 \leqslant Ra \leqslant 10^{10}$, and $0.01 \leqslant Pr \leqslant 0.5$, except for the data set of run 8 at $y = 0.5$ in figure 4(c), which deviates slightly from the scaling law (3.12) owing to the fact that run 8 is for $Pr = 0.5$ and therefore does not sufficiently meet the requirement $Pr < O(1)$ made in the scaling analysis. As can be seen the results fall approximately onto a straight line in all cases, showing that the scaling relations are providing a good representation of the boundary layer in the steady state for these ranges of the control parameters. The numerically quantified forms of these scaling relations are as follows:

$$\tau_{s,y} = 1.988 \left(\frac{1 + Pr}{Pr} \right)^{1/2} y^{1/2}, \tag{3.20}$$

https://doi.org/10.1017/S0022112006003703 Published online by Cambridge University Press

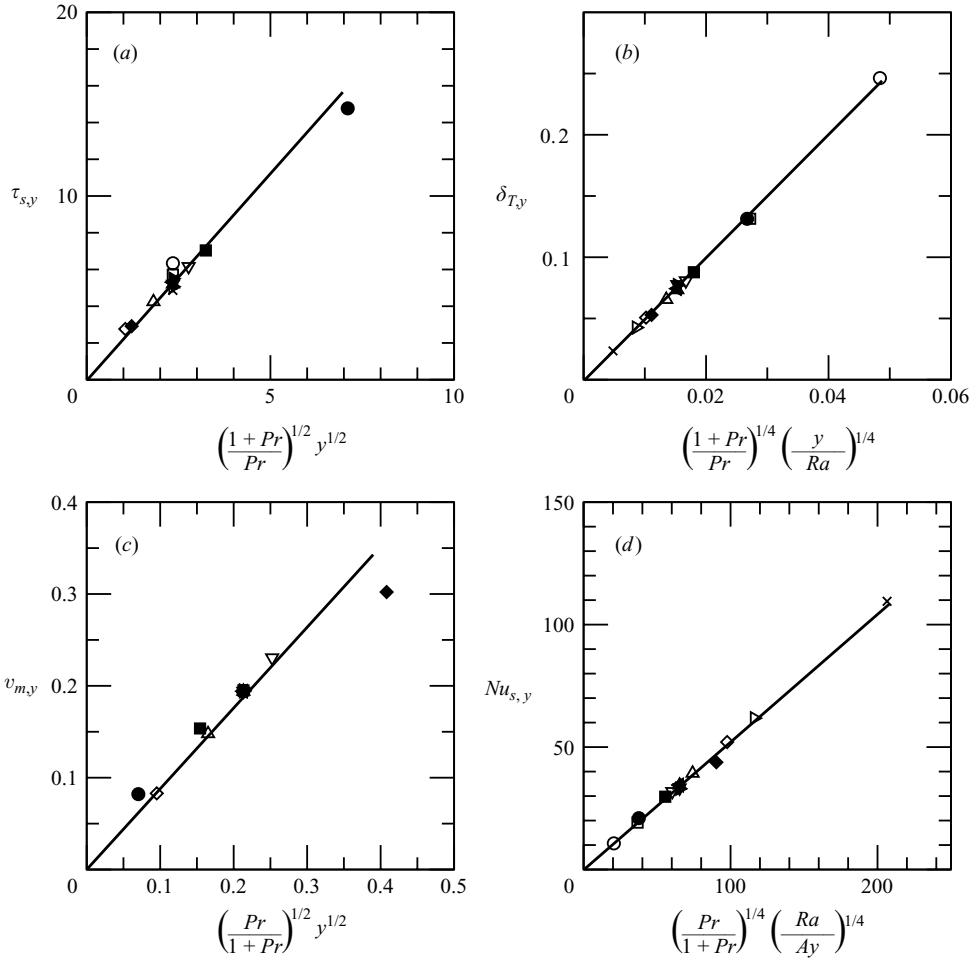


FIGURE 4. (*a*) $\tau_{s,y}$ plotted against $[(1 + Pr)/Pr]^{1/2}y^{1/2}$; (*b*) $\delta_{T,y}$ plotted against $[(1 + Pr)/Pr]^{1/4}y^{1/4}/Ra^{1/4}$; (*c*) $v_{m,y}$ plotted against $[Pr/(1 + Pr)]^{1/2}y^{1/2}$; and (*d*) $Nu_{s,y}$ plotted against $[Pr/(1+Pr)]^{1/4}Ra^{1/4}/y^{1/4}$, for all 12 runs. ○, run 1, $y = 0.5$; □, run 2, $y = 0.5$; ◇, run 3, $y = 0.1$; △, run 3, $y = 0.3$; ◁, run 3, $y = 0.5$; ▽, run 3, $y = 0.7$; ▷, run 4, $y = 0.5$; ×, run 5, $y = 0.5$; ●, run 6, $y = 0.5$; ■, run 7, $y = 0.5$; ◆, run 8, $y = 0.5$; ▲, run 9, $y = 0.5$; ◄, run 10, $y = 0.5$; ▼, run 11, $y = 0.5$; ►, run 12, $y = 0.5$. Solid line, linear fit.

$$\delta_{T,y} = 5.076 \left(\frac{1+Pr}{Pr}\right)^{1/4} \frac{y^{1/4}}{Ra^{1/4}}, \tag{3.21}$$

$$v_{m,y} = 0.698 \left(\frac{Pr}{1+Pr}\right)^{1/2} y^{1/2}, \tag{3.22}$$

$$Nu_{s,y} = 0.529 \frac{Ra^{1/4}}{Ay^{1/4}} \left(\frac{Pr}{1+Pr}\right)^{1/4}, \tag{3.23}$$

$$Nu_{s} = 0.692 \frac{Ra^{1/4}}{A} \left(\frac{Pr}{1+Pr}\right)^{1/4}. \tag{3.24}$$

https://doi.org/10.1017/S0022112006003703 Published online by Cambridge University Press

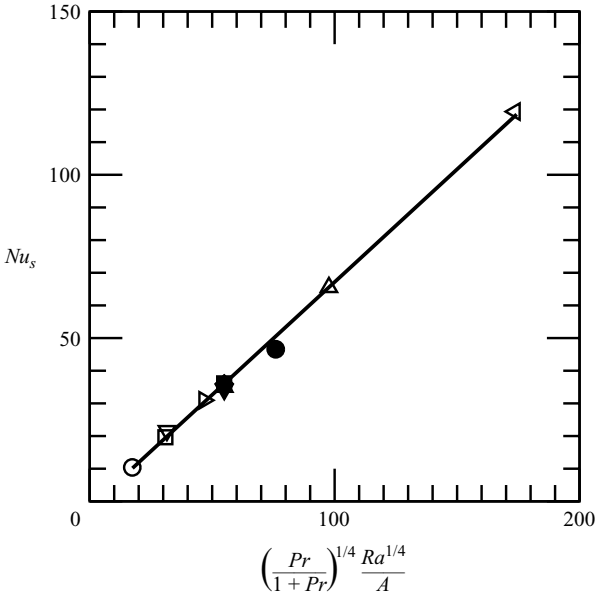


FIGURE 5. Nu_s plotted against $[Pr/(1+Pr)]^{1/4}Ra^{1/4}$ for all 12 runs. ○, run 1; □, run 2; ◇, run 3; △, run 4; ◁, run 5; ▽, run 6; ▷, run 7; ●, run 8; ■, run 9; ◆, run 10; ▲, run 11; ▼, run 12. Solid line, linear fit.

The numerical results for $\delta_T/\delta_{T,y}$, $v_m/v_{m,y}$, $Nu_y/Nu_{s,y}$, and Nu/Nu_s are plotted against $(\tau/\tau_{s,y})^{1/2}$, $\tau/\tau_{s,y}$, $(\tau/\tau_{s,y})^{-1/2}$, and $(\tau/\tau_{s,1})^{-1/2}$ in figures 6 and 7 respectively. The results for $\tau/\tau_{s,y} < 1$ and $\tau/\tau_{s,1} < 1$ fall onto straight lines, showing the validity of the scaling relations at the start-up stage of the boundary-layer development. For $\tau/\tau_{s,y} \geqslant 1$ and $\tau/\tau_{s,1} \geqslant 1$ the results fall onto horizontal lines, showing no time dependence, as is expected. The numerically quantified scaling relations are therefore

$$\delta_T = 1.090\delta_{T,y}\left(\frac{\tau}{\tau_{s,y}}\right)^{1/2} = 3.924\frac{\tau^{1/2}}{Ra^{1/4}}, \tag{3.25}$$

$$v_m = 1.229v_{m,y}\frac{\tau}{\tau_{s,y}} = 0.858\left(\frac{Pr}{1+Pr}\right)\tau, \tag{3.26}$$

$$Nu_y = 0.695Nu_{s,y}\left(\frac{\tau}{\tau_{s,y}}\right)^{-1/2} = 0.518\frac{Ra^{1/4}}{A\tau^{1/2}}, \tag{3.27}$$

$$Nu = 0.743Nu_s\left(\frac{\tau}{\tau_{s,1}}\right)^{-1/2} = 0.725\frac{Ra^{1/4}}{A\tau^{1/2}}, \tag{3.28}$$

and clearly validate the scaling relations (3.6)–(3.8).

The Prandtl-number scaling for the boundary-layer thicknesses at the steady state, i.e. (3.11), (3.13) and (3.14), was examined in detail by plotting the horizontal profiles of temperature and vertical velocity against $x[Pr/(1+Pr)]^{1/4}$, as shown in figure 8, where both raw and scaled results are presented for a range of Pr. The scaling is seen to perform well for the temperature profiles, all profiles collapsing almost onto a single line. This scaling is also seen to work well for the overall thickness of the viscous boundary layer, all results except for $Pr = 0.01$ having a scaled thickness of approximately 0.04, slightly less than that of the thermal boundary-layer thickness.

https://doi.org/10.1017/S0022112006003703 Published online by Cambridge University Press

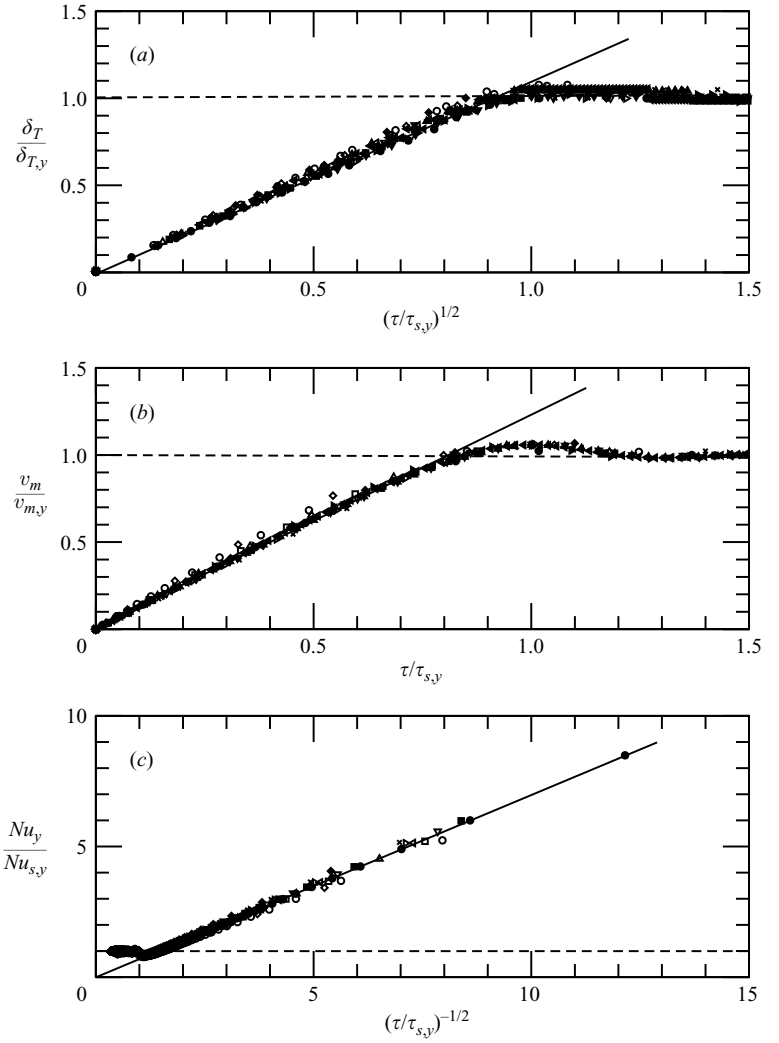


FIGURE 6. Numerical results for (*a*) $\delta_T/\delta_{T,y}$ plotted against $(\tau/\tau_{s,y})^{1/2}$; (*b*) $v_m/v_{m,y}$ plotted against $\tau/\tau_{s,y}$; and (*c*) $Nu_y/Nu_{s,y}$ plotted against $(\tau/\tau_{s,y})^{-1/2}$. ○, run 1, $y=0.5$; □, run 2, $y=0.5$; ◇, run 3, $y=0.1$; △, run 3, $y=0.3$; ◁, run 3, $y=0.5$; ▽, run 3, $y=0.7$; ▷, run 4, $y=0.5$; ×, run 5, $y=0.5$; ●, run 6, $y=0.5$; ■, run 7, $y=0.5$; ◆, run 8, $y=0.5$; ▲, run 9, $y=0.5$; ◀, run 10, $y=0.5$; ▼, run 11, $y=0.5$; ▶, run 12, $y=0.5$. Solid line, linear fit for the start-up stage; dashed line, linear fit for the steady-state stage.

However, the scaling is seen to work poorly in the small-x, near-wall, region, a large variation being seen between all profiles in the scaled results. This indicates that the $\delta_{T,y}$ scaling is appropriate for $\delta_{vo,y}$, which is in agreement with the scaling analysis, but that it does not correctly represent the physics of the viscous boundary layer in the near-wall region. The alternative scaling (3.13), which requires the scaling $xPr^{-1/4}(1+Pr)^{-1/4}$, was also examined for the vertical velocity profiles, with the results shown in figure 9. This scaling is seen to perform better in the small-x region, bringing the maximum-absolute-velocity locations close together; however, it performs very poorly in the large-x region. It is therefore impossible to represent the behaviour of the vertical velocity over δ_v using a single scaling. A further demonstration of this

https://doi.org/10.1017/S0022112006003703 Published online by Cambridge University Press

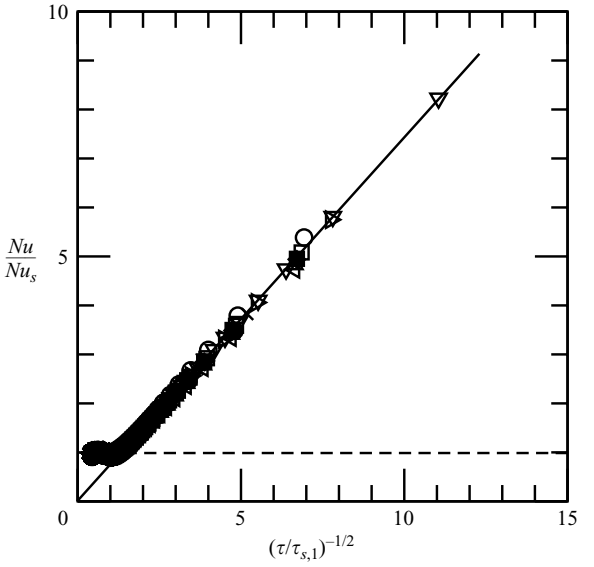


FIGURE 7. Numerical results for Nu/Nu_b plotted against $(\tau/\tau_{s,1})^{-1/2}$. ○, run 1; □, run 2; ◇, run 3; △, run 4; ◁, run 5; ▽, run 6; ▷, run 7; ●, run 8; ■, run 9; ◆, run 10; ▲, run 11; ▼, run 12. Solid line, linear fit.

multiple scaling and the way in which the momentum balances change over time is seen in figure 10, where typical horizontal profiles at $y = 0.5$ of the vertical advection terms $u\partial v/\partial x$, $v\partial v/\partial y$, the buoyancy term $Pr\,\theta$, the viscous term $Pr\,Ra^{-1/2}\partial^2 v/\partial x^2$ and the vertical velocity v are plotted for $\tau = 2$, during the boundary-layer transition (figure 10*a*), and for the fully developed flow at $\tau = 16$ (figure 10*b*). The results are for $Ra = 10^8$, $Pr = 0.1$, and $A = 1$. At early times the buoyancy term reduces slowly with the distance from the wall, whereas the viscous term reduces rapidly and is close to zero at $x = 0.01$. Apart from the near-wall region, where the buoyancy and viscosity terms are in balance, the velocity is clearly accelerated over the full width of the thermal boundary layer by buoyancy, as predicted by (2.8). The advection terms at this time are negligible, again as predicted by the scaling. At steady state the balances have changed; buoyancy is again the primary driving force, acting over the full width of the thermal boundary layer, balanced in the near-wall region by viscosity and away from the wall by the advection terms. The width of the thermal boundary layer is then determined by the convection–conduction balance in the temperature equation. It is thus clear that the flow behaviour cannot be properly represented by a single balance across the full width of the boundary layer.

It can therefore be seen that for small-Pr ($Pr < 1$) fluids the assertion of Incropera & DeWitt (1996, p. 319) and Tritton (1995, p. 170) that the viscous boundary layer should be much thinner than the thermal boundary layer is only valid if this viscous boundary layer is interpreted as the inner viscous boundary layer. The claim is not valid for the outer viscous boundary layer, as it has the same order of thickness as the thermal boundary layer and the ratio of their thicknesses is approximately constant for $Pr < 1$, which supports the claim made by Gebhart *et al.* (1988, p. 53).

3.3.2. *Cooling-down stage*

The time for complete cooling τ_f was determined as the time at which $\theta_a(\tau_f) = -0.99$. The τ_f results are plotted against $[(1 + Pr)/Pr]^{1/4} Ra^{1/4}/A$ in figure 11, which

https://doi.org/10.1017/S0022112006003703 Published online by Cambridge University Press

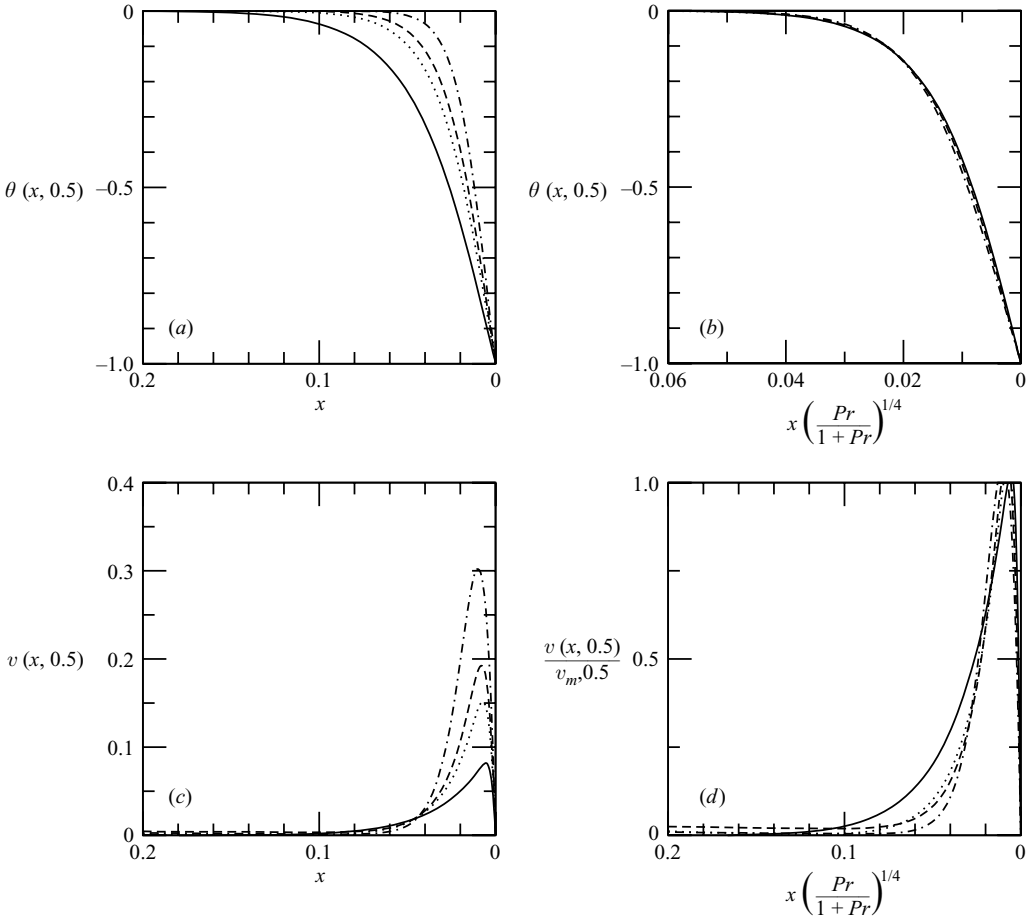


FIGURE 8. Numerical results for the horizontal profiles of temperature $\theta(x, 0.5)$ and vertical velocity $v(x, 0.5)$ at $y = 0.5$ for various Pr values: (*a*) $\theta(x, 0.5)$ plotted against x; (*b*) $\theta(x, 0.5)$ plotted against $x[Pr/(1+Pr)]^{1/4}$; (*c*) $v(x, 0.5)$ plotted against x; (*d*) $v(x, 0.5)/v_m$ plotted against $x[Pr/(1 + Pr)]^{1/4}$ for $Ra = 10^8$ and $A = 1$. —, $Pr = 0.01$; ····, $Pr = 0.05$; – – –, $Pr = 0.1$; – · –, $Pr = 0.5$.

show that all results fall onto approximately the same line, described by

$$\tau_f = 8.34 \left(\frac{1 + Pr}{Pr} \right)^{1/4} \frac{Ra^{1/4}}{A}, \tag{3.29}$$

confirming that this is the appropriate scaling for this phase of the flow. It may be noted that the $A = 1/3$ result is slightly above the best-fit straight line. The cooling-down time is determined by the heat flux through the natural-convection boundary layer. The wave activity within the domain, resulting from the reflection of the intrusion from the symmetry boundary, perturbs the boundary layer and acts to increase the heat flux. For smaller aspect ratios the boundary layer is further removed from the symmetry boundary and subjected to less associated wave activity, reducing the heat flux and increasing the cool-down time in a manner not taken into account in the scaling.

https://doi.org/10.1017/S0022112006003703 Published online by Cambridge University Press

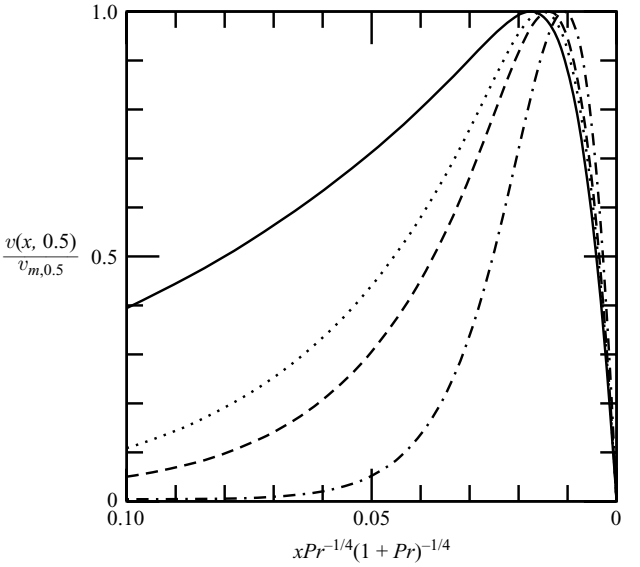


FIGURE 9. Numerical results for the horizontal profiles of the vertical velocity ratio $v(x, 0.5)/v_m$ at $y = 0.5$ plotted against $x(1 + Pr)^{-1/4}Pr^{-1/4}$ for various Pr with $Ra = 10^8$ and $A = 1$. ——, $Pr = 0.01$; · · ·, $Pr = 0.05$; – – –, $Pr = 0.1$; – · – $Pr = 0.5$.

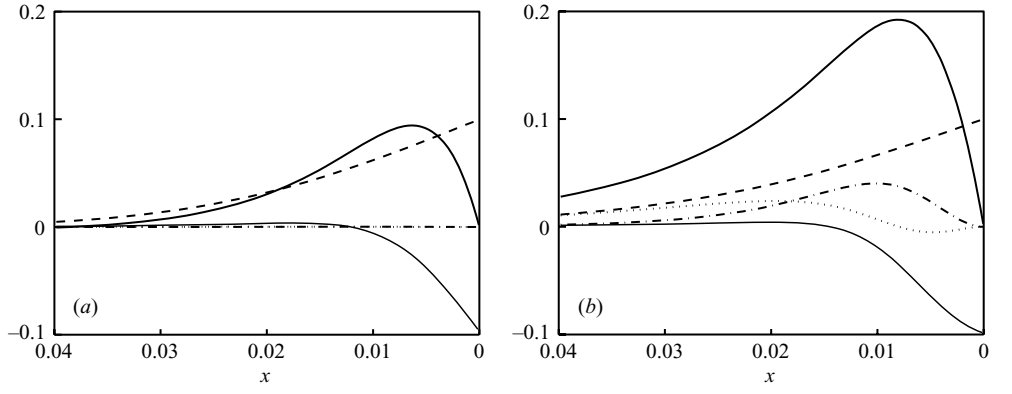


FIGURE 10. Numerically simulated horizontal profiles of the horizontal advection term $u\partial v/\partial x$ (· · · · · ·), the vertical advection term $v\partial v/\partial y$ (– · –), the viscous term $PrRa^{-1/2}\partial^2 v/\partial x^2$ (thin solid line), the buoyancy term $Pr\theta$ (– – –), and the vertical velocity v (thick solid line) at height $y = 0.5$ for $Ra = 10^8$, $Pr = 0.1$, and $A = 1$: (*a*) profiles for $\tau = 2$ (at the start-up stage of the boundary-layer development) and (*b*) profiles for $\tau = 16$ (at the steady state of the boundary-layer development).

Equation (3.29) gives $C_f = 2.067 \times 10^{-4}$. Therefore the full expression for θ_a, from (3.18), is obtained as

$$\theta_a(\tau) = 2.067 \times 10^{-4} \left[\frac{A}{Ra^{1/4}} \left(\frac{Pr}{1 + Pr} \right)^{1/4} (\tau_f - \tau) \right]^4 - 1. \tag{3.30}$$

Figure 12 presents the numerically obtained $\theta_a(\tau)$ for all 12 runs to show the dependence of the scaling relation (3.18) on the individual control parameters Ra,

https://doi.org/10.1017/S0022112006003703 Published online by Cambridge University Press

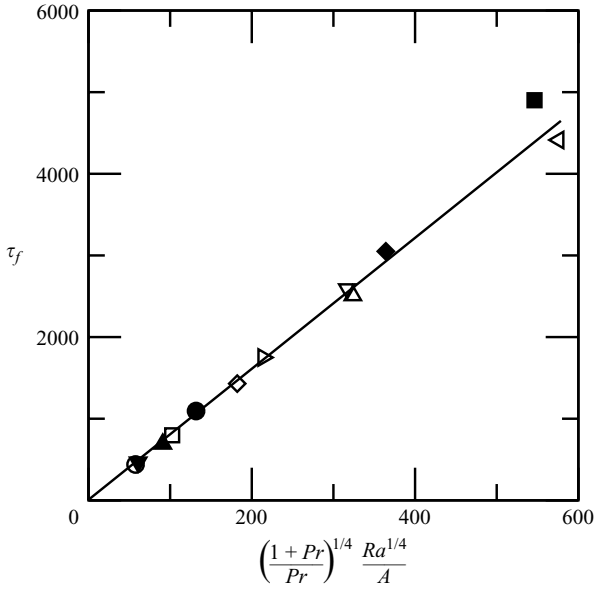


FIGURE 11. The time for complete cooling τ_f plotted against $[(1 + Pr)/Pr]^{1/4}Ra^{1/4}/A$ for all 12 runs. ○, run 1; □, run 2; ◇, run 3; △, run 4; ◁, run 5; ▽, run 6; ▷, run 7; ●, run 8; ■, run 9; ◆, run 10; ▲, run 11; ▼, run 12. Solid line, linear fit.

A, and Pr. Figure 12(a) contains the raw data showing the time series of $\theta_a(\tau)$ for $Ra = 10^6$, 10^7, 10^8, 10^9, and 10^{10} with $A = 1$ and $Pr = 0.1$. The scaling relation (3.18) shows that the dependence of $\theta_a(\tau)$ on Ra goes as $Ra^{-\frac{1}{4}}$, and the time series of $\theta_a(\tau)$ with this scaling are shown in figure 12(b), where it is seen that this scale brings all five sets of data for different Ra together, indicating that $Ra^{-\frac{1}{4}}$ is the correct dependence of $\theta_a(\tau)$ on Ra in the scaling relation (3.18). Similarly, figure 12(c) contains the raw data showing the time series of $\theta_a(\tau)$ for $A = 1/3$, $1/2$, 1, 2, and 3 with $Ra = 10^8$ and $Pr = 0.1$. The scaling relation (3.18) shows that the dependence of $\theta_a(\tau)$ on A goes as A, and the time series of $\theta_a(\tau)$ with this scaling are shown in figure 12(d), where, again, it is seen that the scale brings all five sets of data for different A together, indicating that A itself is the correct dependence of $\theta_a(\tau)$ on A in the scaling relation (3.18). Figure 12(e) contains the raw data showing the time series of $\theta_a(\tau)$ for $Pr = 0.01$, 0.05, 0.1, and 0.5 with $Ra = 10^8$ and $A = 1$. The scaling relation (3.18) shows that the dependence of $\theta_a(\tau)$ on Pr goes as $[Pr/(1 + Pr)]^{1/4}$, and the time series of $\theta_a(\tau)$ with this scaling are shown in figure 12(f), where all four sets of data for different Pr overlay each other, clearly showing that $[Pr/(1 + Pr)]^{1/4}$ is the correct dependence of $\theta_a(\tau)$ on Pr in the scaling relation (3.18).

The numerically obtained $\theta_a(\tau)$ is plotted against $A[Pr/(1 + Pr)]^{1/4}Ra^{-1/4}\tau$ in figure 13(a) for all runs. The collapse of all sets of data onto approximately a single curve again confirms that the scaling relation (3.18) is true. The scaling for the full development of the average temperature is (3.30). This scaling was examined again by plotting the results for the time development of $\theta_a(\tau)$ versus $A^4[Pr/(1+Pr)]Ra^{-1}(\tau_f - \tau)^4$ for all runs, as shown in figure 13(b). There is seen to be some variation in the scaled development; however, it is seen that (3.30) provides a good description of the overall development of $\theta_a(\tau)$.

https://doi.org/10.1017/S0022112006003703 Published online by Cambridge University Press

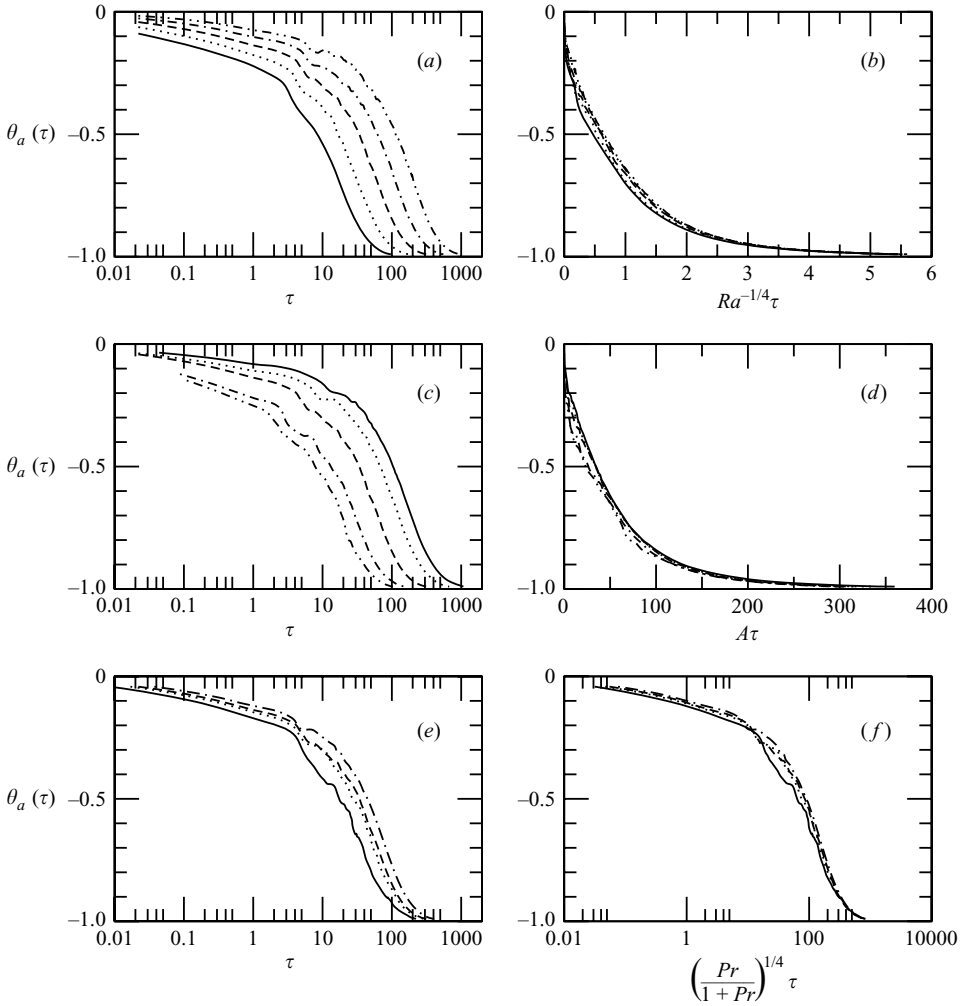


FIGURE 12. (*a*) Time series for the average dimensionless fluid temperature $\theta_a(\tau)$ and (*b*) $\theta_a(\tau)$ plotted against $Ra^{-1/4}\tau$, for $Ra = 10^6$ (——), 10^7 (· · ·), 10^8 (– – –), 10^9 (– · –), and 10^{10} (– · · –) with $A = 1$ and $Pr = 0.1$; (*c*) time series of $\theta_a(\tau)$ and (*d*) $\theta_a(\tau)$ plotted against $A\tau$; for $A = 1/3$ (——), 1/2 (· · ·), 1 (– – –), 2(– · –), and 3 (– · · –) with $Ra = 10^8$ and $Pr = 0.1$; (*e*) time series of $\theta_a(\tau)$ and (*f*) $\theta_a(\tau)$ plotted against $[Pr/(1+Pr)]^{1/4}\tau$, for $Pr = 0.01$ (——), 0.05 (· · ·), 0.1 (– – –), and 0.5 (– · –) with $Ra = 10^8$ and $A = 1$.

The numerical results showing the dependence of the instantaneous average Nusselt number Nu on Ra, A, and Pr at the boundary-layer development stage and at the cooling-down stage are respectively presented in figure 14(*a*) and figure 14(*b*). The results in figure 14(*a*) confirm the scaling relation (3.8) at the boundary-layer development stage, as represented by (3.27), whereas the results in figure 14(*b*) validate the scaling relation (3.19) at the cooling-down stage, which is found to be quantified by the following expression:

$$Nu = 2.708 \times 10^{-5} \frac{Ra^{1/4}}{A} \left(\frac{Pr}{1+Pr}\right)^{1/4} \left(1 - \frac{\tau}{\tau_f}\right)^3. \tag{3.31}$$

https://doi.org/10.1017/S0022112006003703 Published online by Cambridge University Press

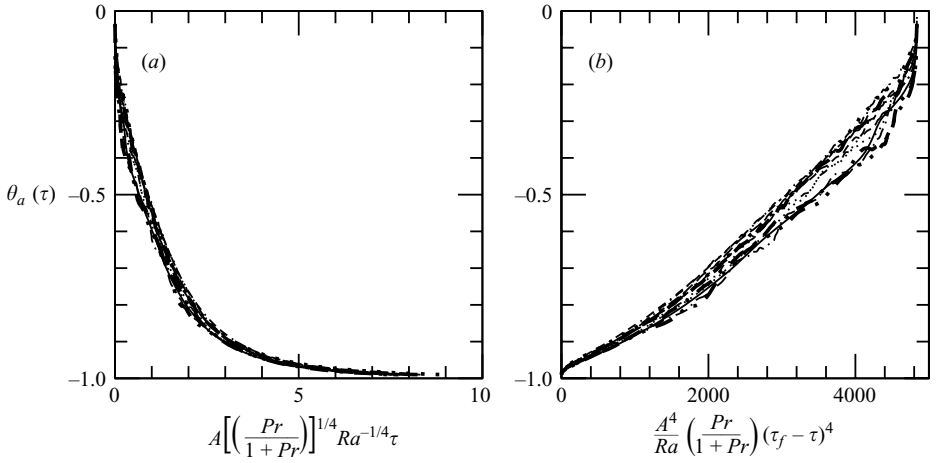


FIGURE 13. $\theta_a(\tau)$ plotted against (*a*) $A[Pr/(1+Pr)]^{1/4}Ra^{-1/4}\tau$ and (*b*) $A^4[Pr/(1+Pr)]Ra^{-1}(\tau_f-\tau)^4$ for all 12 runs.

4. Conclusions

The cooling-down behaviour of a fluid contained in a two-dimensional rectangular enclosure subjected to isothermal boundary conditions on the vertical walls has been examined via scaling analysis and direct numerical simulation. Scaling relations have been obtained for the properties of the initial vertical boundary-layer development and of the cooling-down stage.

The numerical results have confirmed the scaling relations, provided scaling constants, and illustrated the overall flow development. The results presented in figure 8 show that the total (outer) vertical-velocity boundary-layer thickness has the same scaling as that of the thermal boundary-layer thickness; however this scaling performs poorly in the near-wall, inner, region. In this region the alternative scaling $xPr^{-1/4}(1+Pr)^{-1/4}$ is appropriate. This scaling is obtained by assuming that buoyancy balances the horizontal diffusion of vertical velocity in the vertical momentum equation, which gives an inner-velocity boundary-layer thickness δ_{vi} that scales with $Pr^{1/2}\delta_T$, the same scaling as that obtained for this quantity for $Pr > 1$ and, suggested by Incropera & DeWitt (1996, p. 319) and Tritton (1995, p. 170) for small-Pr ($Pr < 1$) fluids. However, for $Pr < 1$ this balance only exists in the near-wall region, where $\partial^2 v/\partial x^2$ is positive. In the outer region the flow is driven in the same direction via viscous effects and buoyancy; these quantities have the same sign and a balance will exist between them and inertia, providing a different scaling. It is therefore not possible to obtain a single scaling for the velocity structure over the full velocity boundary-layer width. Nonetheless it is clear that for $Pr < 1$ the overall (outer) velocity boundary-layer thickness has the same scaling and approximately the same magnitude as the thermal boundary-layer thickness, supporting the statement of Gebhart *et al.* (1988).

Although numerical results have been presented only for two-dimensional symmetric flow, three-dimensional results without the assumption of symmetry have been obtained demonstrating that the two-dimensional symmetric assumption is correct. The scalings obtained here can therefore be applied to the equivalent three-dimensional flow.

https://doi.org/10.1017/S0022112006003703 Published online by Cambridge University Press

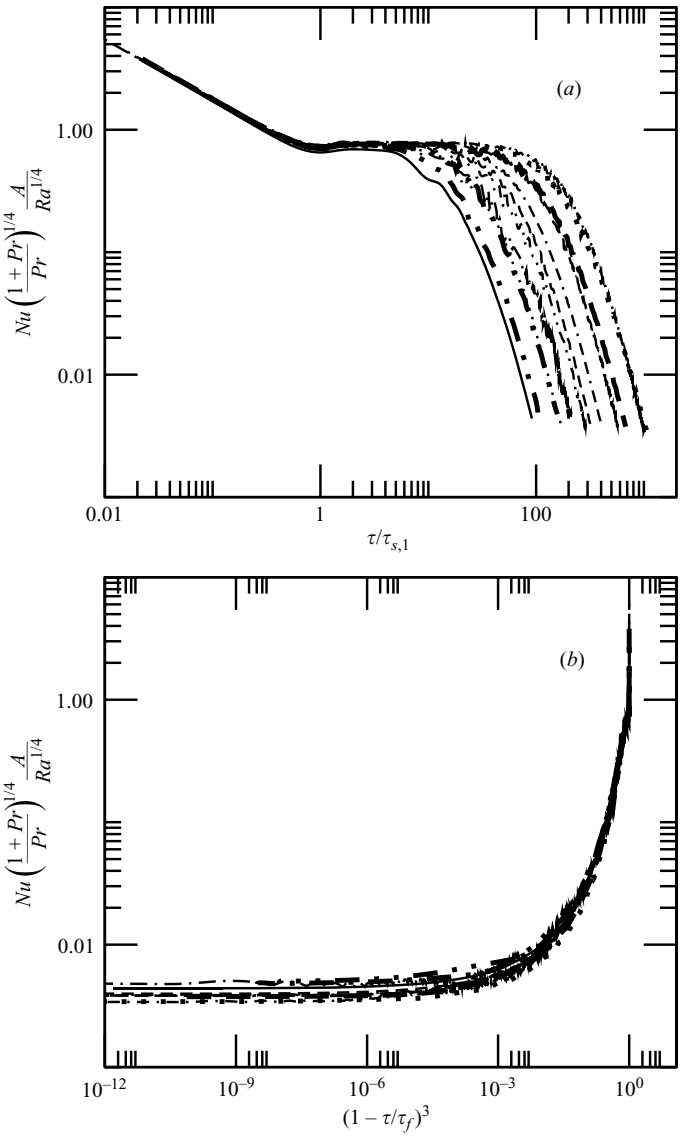


FIGURE 14. $NuA[(1+Pr)/Pr]^{1/4}Ra^{-1/4}$ plotted against (*a*) $\tau/\tau_{s,1}$ and (*b*) $(1-\tau/\tau_f)^3$ for all 12 runs.

The financial support of the Australian Research Council (Grant No. DP0449876), the National Natural Science Foundation of China (Grant No. 10262003), the Natural Science Foundation of Yunnan Province of China (Key Project, Grant No. 2003E0004Z), and the Program for New Century Excellent Talents in the University of China (Grant No. NCET-04-0918) are gratefully acknowledged.

REFERENCES

ARMFIELD, S. W. 1991 Finite-difference solutions of the Navier–Stokes equations on staggered and non-staggered grids. *Computers Fluids* **20**, 1–17.

ARMFIELD, S. W. & DEBLER, W. 1993 Purging of density stabilized basins. *Intl J. Heat Mass Transfer* **36**, 519–530.

https://doi.org/10.1017/S0022112006003703 Published online by Cambridge University Press

Armfield, S. W. & Patterson, J. C. 1991 Direct simulation of wave interactions in unsteady natural convection in a cavity. *Intl J. Heat Mass Transfer* **34**, 929–940.

Armfield, S. W. & Patterson, J. C. 1992 Wave properties of natural-convection boundary layers. *J. Fluid Mech.* **239**, 195–211.

Armfield, S. W. & Street, R. L. 1999 The fractional-step method for the Navier–Stokes equations on staggered grids: the accuracy of three variations. *J. Comput. Phys.* **153**, 660–665.

Catton, I. 1978 Natural convection in enclosures. In *Proc. 6th Intl Heat Transfer Conf.*, pp. 13–43.

Gebhart, B., Jaluria, Y., Mahajan, R. L. & Sammakia, B. 1988 *Buoyancy-Induced Flows and Transport*. Hemisphere.

Goldstein, R. J. & Briggs, D. G. 1964 Transient free convection about vertical plates and circular cylinders. *Trans. ASME: J. Heat Transfer* **86**, 490–500.

Goldstein, R. J., Eckert, E. R. G., Ibele, W. E. *et al.* 2003 Heat transfer – a review of 2001 literature. *Intl J. Heat Mass Transfer* **46**, 1887–1992.

Hyun, J. M. 1984 Transient process of thermally stratifying an initially homogeneous fluid in an enclosure. *Intl J. Heat Mass Transfer* **27**, 1936–1938.

Hyun, J. M. 1985 Effect of the Prandtl number on heatup of a stratified fluid in a enclosure. *Trans. ASME: J. Heat Transfer* **107**, 982–984.

Hyun, J. M. 1994 Unsteady buoyant convection in an enclosure. *Adv. Heat Transfer* **24**, 277–320.

Incropera, F. P. & DeWitt, D. P. 1996 *Fundamentals of Heat and Mass Transfer*, 4th Edn. John Wiley & Sons.

Javam, A., Imberger, J. & Armfield, S. W. 1999 Numerical study of internal wave reflection from sloping boundaries. *J. Fluid Mech.* **396**, 183–201.

Kwak, H. S., Kuwahara, K. & Hyun, J. M. 1998 Convective cool-down of a contained fluid through its maximum density temperature. *Intl J. Heat Mass Transfer* **41**, 323–333.

Leonard, B. P. 1979 A stable and accurate convective modelling procedure based on quadratic upstream interpolation. *Comp. Meth. Appl. Mech. Engng* **19**, 59–98.

Lin, W. 2000 Scaling analysis and direct simulation of unsteady weak fountains and natural convection flow. PhD Thesis, The University of Sydney, Sydney.

Lin, W. & Armfield, S. W. 1999 Direct simulation of natural convection cooling in a vertical circular cylinder. *Intl J. Heat Mass Transfer* **42**, 4117–4130.

Lin, W. & Armfield, S. W. 2000 Direct simulation of weak axisymmetric fountains in a homogeneous fluid. *J. Fluid Mech.* **403**, 67–88.

Lin, W. & Armfield, S. W. 2001 Natural convection cooling of rectangular and cylindrical containers. *Intl J. Heat Fluid Flow* **22**, 72–81.

Lin, W. & Armfield, S. W. 2002 Weak fountains in a stratified fluid. *Phys. Rev.* E **66**, 066308.

Lin, W. & Armfield, S. W. 2003 The Reynolds and Prandtl number dependence of weak fountains. *Computational Mech.* **31**, 379–389.

Lin, W. & Armfield, S. W. 2004 Long-term behaviour of cooling fluid in a rectangular container. *Phys. Rev.* E **69**, 056315.

Nicolette, V. F. & Yang, K. T. 1985 Transient cooling by natural convection in a two-dimensional square enclosure. *Intl J. Heat Mass Transfer* **28**, 1721–1732.

Ostrach, S. 1953 An analysis of laminar free-convection flow and heat transfer about a flat plate parallel to the direction of the generating body force. *NACA Rep.* 1111.

Ostrach, S. 1982 Natural convection heat transfer in cavities and cells. In *Proc. 7th Intl Heat Transfer Conf.*, pp. 365–379.

Otis, D. R. & Roessler, J. 1987 Development of stratification in a cylindrical enclosure. *Intl J. Heat Mass Transfer* **30**, 1633–1636.

Patterson, J. C. 1984. Unsteady natural convection in a cavity with internal heating and cooling. *J. Fluid Mech.* **140**, 135–151.

Patterson, J. C. & Armfield, S. W. 1990 Transient features of natural convection in a cavity. *J. Fluid Mech.* **219**, 469–497.

Patterson, J. C. & Imberger, J. 1980. Unsteady natural convection in a rectangular cavity. *J. Fluid Mech.* **100**, 65–86.

Schladow, S. G., Patterson, J. C. & Street, R. L. 1989 Transient flow in a side-heated cavity at high Rayleigh number: a numerical study. *J. Fluid Mech.* **200**, 121–148.

Tritton, D. J. 1995 *Physical Fluid Dynamics*, 2nd Edn. Oxford University Press.

https://doi.org/10.1017/S0022112006003703 Published online by Cambridge University Press